rides is more difficult than that of the alkoxo ligands. Nevertheless, the permittivities of these films are only slightly lower than those of the corresponding materials deposited by the conventional ALD processes, and their leakage current properties are nearly identical (*21*). For removal of the chloride residues, proper post-deposition annealing conditions must be looked for in which the chlorides are replaced by oxygen but the underlying silicon is not yet oxidized. In contrast, the use of metal iodides with weaker binding energies than the chlorides offers a potential way to decrease the halide residues. Yet another scheme might be to use this new process only for the interface formation and then continue with the conventional ALD processes, which leave fewer residues.

Whereas the reactions between the halides and alkoxides were known from the solution studies, the success of depositing Al_2O_3 from aluminium isopropoxide and trimethyl aluminium was more surprising. Most likely this reaction mechanism involves formation of *tert*-butane

$$Al(CH_3)_3 + Al(OCH(CH_3)_2)_3 \rightarrow Al_2O_3 + 3\ CH_3CH(CH_3)_2 \quad (4)$$

The most important finding related to this ALD chemistry is that there is no interfacial silicon oxide layer between the silicon substrate and an Al_2O_3 film (Fig. 1). Before depositing this film, the silicon surface was etched with a dilute aqueous HF solution to remove the native oxide and to leave the surface hydrogen terminated. Whether the thin light zone at the interface is real or is an artifact is impossible to distinguish. However, even if the interface does have oxidized silicon, it is only one monolayer thick and, thus, represents an atomic-level interface between Al_2O_3 and Si, which is oxidized only from its topmost layer. The absence of a thicker interfacial layer implies that ALD with the use of alkoxides as oxygen sources is a viable technique for gate oxide deposition for the future-generation integrated circuits. The other requirements for the gate oxide deposition method, i.e., accurate thickness control and uniformity over the large silicon wafers, are inherently fulfilled by ALD because of its self-limiting film growth process.

References and Notes

1. G. Moore, *IEDM Tech. Dig.* (1975), p. 11.
2. Semiconductor Industry Association, *National Technology Roadmap for Semiconductors: Technology Needs* (Sematech, Austin, TX, 1997). See also www.itrs.net/ntrs/publntrs.nsf.
3. M. Schulz, *Nature* **399**, 729 (1999)
4. P. A. Packan, *Science* **285**, 2079 (1999)
5. D. A. Muller *et al.*, *Nature* **399**, 758 (1999).
6. The gate metal-oxide-semiconductor structure may be thought of as a parallel plate capacitor with capacitance $C = \varepsilon_r\varepsilon_0 A/d$, where ε_r is the relative permittivity of the oxide, ε_0 is the permittivity of a vacuum, A is the area of the capacitor, and d is the thickness of the oxide.
7. K. J. Hubbard and D. G. Schlom, *J. Mater. Res.* **11**, 2757 (1996).
8. G. D. Wilk and R. M. Wallace, *Appl. Phys. Lett.* **74**, 2854 (1999)
9. R. A. McKee, F. J. Walker, M. F. Chisholm, *Phys. Rev. Lett.* **81**, 3014 (1998)
10. L. Niinistö, M. Ritala, M. Leskelä, *Mater. Sci. Eng. B* **41**, 23 (1996).
11. M. Ritala, *Appl. Surf. Sci.* **112**, 223 (1997).
12. J. W. Klaus, O. Sneh, S. M. George, *Science* **278**, 1934 (1997)
13. J. W. Klaus, O. Sneh, A. W. Ott, S. M. George, *Surf. Rev. Lett.* **6**, 435 (1999).
14. M. Ritala *et al.*, *Chem. Vap. Deposition* **5**, 7 (1999).
15. R. Corriou, D. Leclercq, P. Lefèrve, P. H. Mutin, A. Vioux, *Chem. Mater.* **4**, 961 (1992).
16. A. Vioux, *Chem. Mater.* **9**, 2292 (1997).
17. T. J. Trentler, T. E. Denler, J. F. Bertone, A. Agrawal, V. L. Colvin, *J. Am. Chem. Soc.* **121**, 1613 (1999).
18. The films were deposited in a flow type F-120 ALD reactor (Microchemistry, Espoo, Finland) operated under a pressure of about 10 mbar. Nitrogen was used as a carrier and as a purging gas. The compounds $Al(CH_3)_3$ and $Si(OEt)_4$ were evaporated in external sources and led into the reactor through a solenoid valve. The other compounds were evaporated inside the reactor at temperatures that correspond to a vapor pressure of about 0.1 mbar. The source vapors were pulsed onto the substrates by means of inert gas valving. Glass and silicon were used as substrates. Film thicknesses were evaluated from transmission spectra, and elemental analyses were carried out at the accelerator laboratory in Helsinki by TOF-ERDA with the use of 53-MeV $^{127}I^{10+}$ ions as projectiles.
19. L. Bourget, R. J. P. Corriou, D. Leclercq, P. H. Mutin, A. Vioux, *J. Non-Cryst. Solids* **242**, 81 (1998).
20. *Outokumpu HSC Chemistry for Windows* program, version 4.0, Outokumpu Research Oy, Pori, Finland.
21. For comparison with the conventional ALD processes, the dielectric properties were mainly measured with In_2O_3:Sn-insulator-Al capacitor structures because that was the standard procedure in earlier studies. The insulators were made 100 to 200 nm thick so that the measured permittivity and leakage reflect the properties of the film bulk rather than the interfaces in these specific capacitors. For an Al_2O_3 film made by the new process from $AlCl_3$ and $Al(O^iPr)_3$, a permittivity of 7.5 and a leakage current density of 10^{-7} A/cm^2 at an electric field of 2.0 MV/cm were measured. The corresponding values for an Al_2O_3 film made by the conventional ALD process from $Al(CH_3)_3$ and H_2O were 8.2 and 10^{-6} A/cm^2 for the permittivity and the leakage current density, respectively. Likewise, Ta_2O_5 made from $TaCl_5$ and $Ta(OEt)_5$ had a permittivity of 20 to 24, whereas the conventional processes result in permittivities of 24 to 25 (Et, ethyl). The leakages in these films were on equivalent levels. The $Zr_{0.45}Ti_{0.55}O_2$ film deposited at 300°C with the new chemistry was partly crystallized and had a high permittivity of 43, but, like the high permittivity materials in general, it possessed a rather high leakage current of 10^{-6} A/cm^2 at an electric field of 0.2 MV/cm. In contrast, when deposited at 250°C, the film was completely amorphous, had a permittivity of 17, and had a greatly reduced leakage such that the level of 10^{-6} A/cm^2 was achieved with an electric field of only 1 to 2 MV/cm. However, with this material, no direct comparison to the conventional ALD processes can be made.

22. Supported by the Academy of Finland and the Finnish National Technology Agency (TEKES).

6 December 1999; accepted 24 February 2000

Nanometer-Size α-PbO_2–Type TiO_2 in Garnet: A Thermobarometer for Ultrahigh-Pressure Metamorphism

Shyh-Lung Hwang,[1] Pouyan Shen,[2]* Hao-Tsu Chu,[3] Tzen-Fu Yui[4]

A high-pressure phase of titanium dioxide (TiO_2) with an α-PbO_2–type structure has been identified in garnet of diamondiferous quartzofeldspathic rocks from the Saxonian Erzgebirge, Germany. Analytical electron microscopy indicates that this α-PbO_2–type TiO_2 occurred as an epitaxial nanometer-thick slab between twinned rutile bicrystals. Given a V-shaped curve for the equilibrium phase boundary of α-PbO_2–type TiO_2 to rutile, the stabilization pressure of α-PbO_2–type TiO_2 should be 4 to 5 gigapascals at 900° to 1000°C. This suggests a burial of continental crustal rocks to depths of at least 130 kilometers. The α-PbO_2–type TiO_2 may be a useful pressure and temperature indicator in the diamond stability field.

Coesite or diamond inclusions in garnet are important indicators of ultrahigh-pressure (UHP) metamorphism [above 2.5 to 2.7 GPa for the production of coesite (*1*)] in orogenic belts such as the western Alps (*2*), the Kokchetav Massif in Kazakhstan (*3, 4*), Dabie Shan in central China (*5*), the western Gneiss Region in Norway (*6*), and recently the Saxonian Erzgebirge in Germany (*7*). UHP metamorphism is important to our understanding of continental collision zones and the mantle dynamics attending subduction (*1*). For example, the source rocks in the Kokchetav Massif (*4*) and the Saxonian Erzgebirge (*7*) are acidic crustal rocks, and as such they imply burial to the mantle depths before exhumation to the surface. In general, inclusions larger than several micrometers in diameter can be identified using optical microscopy, Raman probe, or electron probe microanalysis, as well as methods for polishing thin rock sections to quanti-

[1]Department of Materials Science and Engineering, I-Shou University, Kaohsiung, Taiwan, ROC. [2]Institute of Materials Science and Engineering, National Sun Yat-sen University, Kaohsiung, Taiwan, ROC. [3]Central Geological Survey, Post Office Box 968, Taipei, Taiwan, ROC. [4]Institute of Earth Sciences, Academia Sinica, Taipei, Taiwan, ROC

*To whom correspondence should be addressed. E-mail: pshen@mail.nsysu.edu.tw

tatively detect microdiamonds that were exposed at the polished surface by the peculiar striation pattern around them (*4*). Here, we report the occurrence of submicrometer-size high-pressure titania polymorph inclusions in garnet of diamondiferous gneiss from the Saxonian Erzgebirge, which were overlooked by the above techniques but can be characterized by analytical electron microscopy (AEM).

The crystalline massif of the Erzgebirge is located in Saxony and the northern Czech Republic. It has a central portion called the gneiss-eclogite unit (GEU), which consists mainly of ortho- and paragneisses with numerous lenses of eclogite. The diamondiferous gneiss discovered by Massonne (*7*) from this unit is near the eastern shore of the Saidenbach reservoir, about 1.5 km northeast of the village of Forchheim. The high-pressure metamorphism there was recently dated at about 340 million years ago (*8*). The diamondiferous gneisses are characterized by abundant quartz, rutile, and phengite, as well as by peculiarly round, relatively large garnets (with diameters in the millimeter range) that amount to 10 to 20% of the bulk rock by volume. In such gneisses, diamonds are enclosed in garnet, kyanite, and zircon (*7*). Microdiamonds and graphite pseudomorphs were found only in the zone of garnet with a relatively high Mg/Ca ratio in comparison to the core and rim. This diamondiferous gneiss was used for the present AEM (*9*) reconnaissance of submicrometer-size inclusions in garnet, in particular within the zone with microdiamond inclusions.

Titania crystals formed submicrometer-size inclusions in porphyroblastic garnet of almandine-rich composition [$Alm_{54-56}Py_{29-36}Gro_{9-15}Sp_1$ according to Massonne's garnet data (*7*), where Py is pyrope, Gro is grossular, and Sp is spessartine]. Electron diffraction analysis indicated that these titania inclusions are mostly {110} faceted rutile having no specific crystallographic relationship to the garnet host. After exploring two garnet crystals in separate AEM specimens, we found one of six submicrometer-scale rutile inclusions to be twinned. This rutile inclusion with dislocations formed twinned bicrystals with a butterfly shape when viewed along the [11$\bar{1}$] zone axis of rutile to show edge-on {110} faces and (011) twin planes (Fig. 1). A distinct slab sandwiched between the twinned rutile bicrystals was found to be wide enough (about 8 nm thick) to be identified edge-on by semiquantitative energy-dispersive x-ray (EDX) analysis and electron diffraction as α-PbO_2–type structure of TiO_2, that is, a columbite phase not previously found in Earth. The EDX analysis on the slab edge-on (*9*) showed mainly the oxygen and titanium counts, with the remaining cation counts from the surrounding garnet matrix and the supporting Mo grid and Cu ring (Fig. 1C). Because the EDX analysis on the twinned rutile apart from the α-PbO_2–structured TiO_2 slab gave the same results, it is reasonable to believe that the two phases have the same composition. This interpretation is supported by later electron diffraction identification of the epitaxial α-PbO_2–structured TiO_2 slab at the rutile twin boundary, indicating martensitic (i.e., isochemical) transformation from rutile.

The identity of α-PbO_2–type structure was verified by selected area electron diffraction (SAED) patterns in $[110]_\alpha/[11\bar{1}]_{rut}$, $[210]_\alpha/[21\bar{1}]_{rut}$, $[310]_\alpha/[31\bar{1}]_{rut}$, and $[100]_\alpha/[100]_{rut}$ (Fig. 2, A to D, respectively, where rut denotes rutile). The four zone-axis patterns with eight measured interplanar spacings (Table 1) and angles between zone-axis patterns (*10*) are consistent with an orthorhombic unit cell, specifically α-PbO_2–type TiO_2 (space group *Pbcn*) (*11*), for the following reasons. First, the observed *d*-spacings, calibrated with the tetragonal cell dimensions [a = 0.4594 nm, c = 0.2959 nm (*12*)] of the coexisting rutile, fit the calculated *d*-spacings of synthetic α-PbO_2–type TiO_2 within 1% (Table 1). The refined orthorhombic cell parameters (*13*) are a = 0.459 ± 0.005 nm, b = 0.544 ± 0.001 nm, c = 0.494 ± 0.002 nm, in close agreement with those of synthetic material quenched to room pressure and temperature (a = 0.4563 ± 0.0016 nm, b = 0.5469 ± 0.0015 nm, c = 0.4911 ± 0.0019 nm) (*11*). Second, the observed diffraction conditions (*14*) allow a unique assignment of the space group *Pbcn* (*15*). The presence of 111 and 121 diffractions excludes nonprimitive orthorhombic space groups. The space groups without glide plane and screw axis have no systematic absences and hence can be excluded.

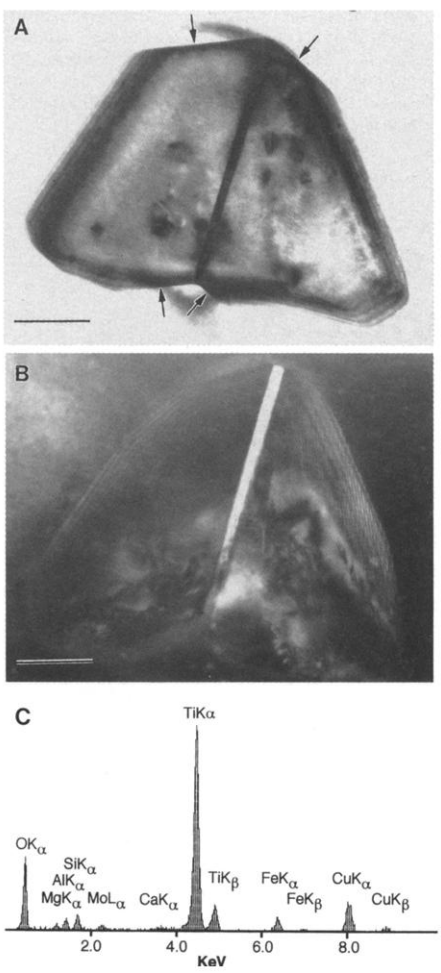

Fig. 1. (**A**) Transmission electron micrograph (bright-field image) of titania inclusion in garnet, consisting of an epitaxial α-PbO_2–type TiO_2 slab sandwiched between twinned rutile bicrystals with a specific crystallographic relationship. Arrows indicate the {110} faces of the rutile crystals. (**B**) Dark-field image of the α-PbO_2–type TiO_2 slab. Scale bar, 50 nm. (**C**) Energy-dispersive x-ray analysis of α-PbO_2–type TiO_2 slab edge-on showing strong Ti and O peaks, with other weak peaks from garnet host and supporting Mo grid and Cu ring.

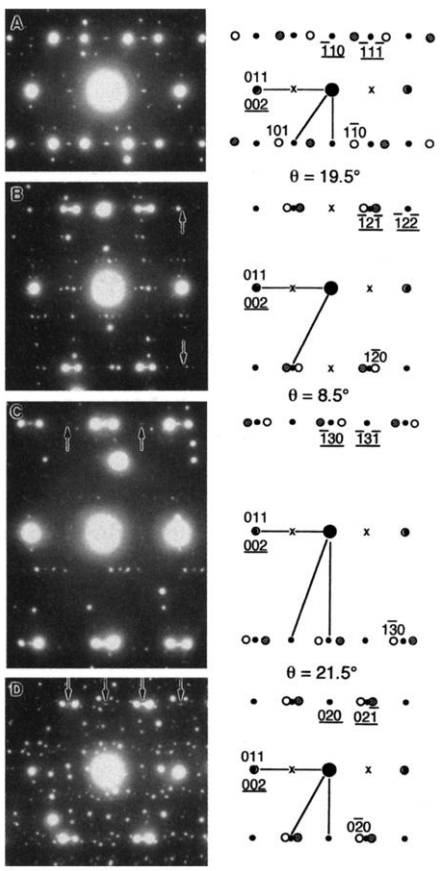

Fig. 2. Selected area diffraction patterns and schematic indexing of twinned rutile (rut) and sandwiched α-PbO_2–type TiO_2 slab in the zone axes of (**A**) $[110]_\alpha/[11\bar{1}]_{rut}$, (**B**) $[\bar{2}10]_\alpha/[21\bar{1}]_{rut}$, (**C**) $[310]_\alpha/[31\bar{1}]_{rut}$, and (**D**) $[100]_\alpha/[100]_{rut}$. Open circles (*hkl*), shaded circles, small solid circles (*hkl*), and crosses denote diffraction spots of rutile, twinned rutile, α-PbO_2–type TiO_2, and allowed double diffractions of α-PbO_2–type TiO_2, respectively. Line segments refer to *d*-spacings compiled in Table 1. Other spots are due to the garnet host or double diffraction of coexisting phases. Arrows indicate diffractions weak in intensity because of a low structure factor (B and C) or a high tilting angle of the thin specimen (D). The tilting angles between zone-axis patterns are also marked.

The presence of 110, 130, and 021 and the absence of 010, 001, 011, and 120 further exclude all other orthorhombic space groups except *Pbcn*. Indeed, the *d*-spacings, interplanar angles, and tilting angles between zone-axis patterns shown in Fig. 2 fit well the synthetic α-PbO_2–type TiO_2 (*11*). The identity of the α-PbO_2–type TiO_2 is also supported by the fact that the slab back-transformed partially into rutile structure after ~20 hours of electron irradiation, hence the dimmed spots of the α-PbO_2–type TiO_2. The α-PbO_2–type TiO_2 (001) slab is parallel to the (011) twin plane of rutile with a specific crystallographic relationship $[100]_\alpha//[100]_{rut}$; $(001)_\alpha//(011)_{rut}$ between them, according to the schematic indexing of the diffraction patterns in Fig. 2. A dark-field imaging using $(020)_\alpha$ diffraction spot near $[100]_\alpha$ zone axis shows the α-PbO_2–type TiO_2 slab in bright contrast (Fig. 1B).

The crystallographic relationship and habit plane between this α-PbO_2–type TiO_2 slab and twinned rutile host can be explained by a martensitic-type transformation (*12*). The structural transition from rutile to α-PbO_2–type structure can be achieved by shearing on the {011} plane of the rutile. The α-PbO_2–type structure can be resolved into rutile-type slabs that are two octahedra wide, bounded by $(001)_\alpha/\{011\}_{rut}$, as depicted in the idealized hexagonal close-packed (hcp) projection along [100] for both phases (Fig. 3) (*12*). These slabs may be in antiphase because the linear chains of filled and empty octahedra, characteristic of rutile, are interchanged across each boundary. A single crystal of rutile subject to shock loading along the ⟨100⟩ direction, which gave the maximum yield of α-PbO_2–type TiO_2 relative to other loading directions, showed the above crystallographic relationship and habit plane between rutile and α-PbO_2–type TiO_2 (*16*). The same crystallographic scheme was used to account for the shock loading behavior of rutile (*16*). The (011) twin boundary of rutile itself is already a basic unit of α-PbO_2–type structure (Fig. 3C). Thus, the epitaxial nucleation of α-PbO_2–type TiO_2 at this twin boundary is crystallographically favored. This also accounts for the absence of α-PbO_2–type TiO_2 slab for the nearby rutile crystals without twinning.

Olsen *et al.* (*17*) used in situ x-ray powder diffraction to reveal the phase transition between rutile and α-PbO_2–type TiO_2. They emphasized the rutile and α-PbO_2–type phase boundary and the nanophase effect (*18*), but unfortunately did not mention the transformation mechanism and the nature of the resulting microstructures for us to compare with the present sample. The bulk rutile sample used by Olsen *et al.* consisted of powders finer than 0.7 μm, and the nanophase TiO_2 sample prepared by milling was about 10 nm, slightly larger than the thickness of α-PbO_2–structured TiO_2 slab in the present study. Because the position of the phase boundary is determined by surface energies of the two phases, the nature of the surface and interface, such as the twin boundary of rutile pertinent to the present sample, should be crucial to the nanophase effect (*18*). According to the "bulk" stability field of α-PbO_2–structured TiO_2 (Fig. 4), the minimum pressure of transition is about 6 GPa and could have been up to 2 GPa lower as a result of the nanophase effect. On the basis of the V-shaped curve for the equilibrium pressure-temperature (*P-T*) phase boundary of α-PbO_2–type TiO_2/rutile (Fig. 4) (*17*), the stabilization pressure of nanometer-size α-PbO_2–type TiO_2 in the present study might be near 4 to 5 GPa at 900° to 1000°C; such metamorphic temperatures were evidenced by incorporation of Ti in garnet (*7*). Because the titania inclusions were not formed during retrograde transformation but during prograde metamorphism, the coexistence of rutile and α-PbO_2–type TiO_2 may suggest a peak metamorphic condition close to the phase boundary. This supports the previous suggestion of a burial of diamondiferous gneisses to depths of at least 130 km (*7*) according to the graphite-diamond transition of Berman (*19*). Indeed, from the geothermobarometric results (which include phengite and garnet composition and textural observations), the *P-T* path for the diamondiferous gneisses of the Saxonian Erzgebirge has been suggested to follow three stages, with the second stage within the diamond stability field (*7*). This stage is consistent with the *P-T* conditions for the equilibrium formation of α-PbO_2–type TiO_2 from nanophase rutile (*17*) (Fig. 4).

Twinning on (011) for rutile bicrystals, commonly found in crustal rocks, is known as geniculated twinning (*20*). The twinned rutile should have been present in the thickened continental crust in metamorphic stage I, and then partially transformed, possibly because of sluggishness of the transition (*17*), to α-PbO_2–type TiO_2 after the graphite-diamond transition in stage II, corresponding to the formation of the diamondiferous intermediate zoning of garnet (*7*). The subsequent exhumation event caused further growth of the garnet and the incorporation of the rutile and α-PbO_2–type TiO_2 assemblage along with diamonds as inclusions in the garnet. Rutile, which has a high isothermal bulk modulus K_T = 210 GPa (*17*) and remains quite stiff at high temperatures (*21*), may exert effective volume constraint during decompression to prevent α-PbO_2–type TiO_2 from back-transformation to rutile in stage III during formation of the garnet rim (*7*). Still, the subduction and exhumation of the continental crust should be rapid enough to partially form and retain the nanometer-size α-PbO_2–type TiO_2 in the twinned rutile bicrystals.

The slope change of the rutile to α-PbO_2–

Table 1. Observed and calculated *d*-spacings for α-PbO_2–type TiO_2. The observed *d*-spacings (± 0.002 nm) were calibrated by coexisting rutile diffraction spots in the SAED patterns of Fig. 2. The calculated *d*-spacings were based on the lattice parameters (a = 0.4563 nm, b = 0.5469 nm, c = 0.4911 nm) of synthetic α-PbO_2–type TiO_2 at room pressure and temperature (*11*). The refined *d*-spacings for the present α-PbO_2–type TiO_2 (a = 0.459 nm, b = 0.544 nm, c = 0.494 nm) are also given.

hkl	*d*-spacing (nm)		
	Observed	Calculated	Refined
110	0.352	0.350	0.351
111	0.287	0.285	0.286
020	0.273	0.274	0.272
002	0.247	0.246	0.247
021	0.240	0.239	0.238
121	0.212	0.212	0.212
130	0.169	0.170	0.169
131	0.159	0.160	0.160

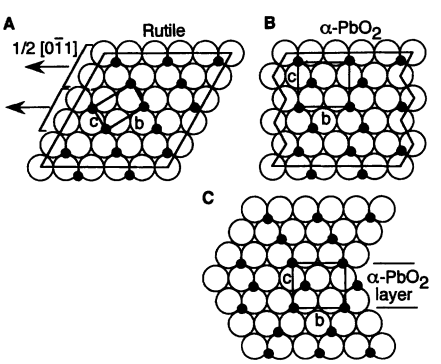

Fig. 3. Schematic drawing of atom positions and crystallographic axes *b* and *c* for (**A**) rutile (b = a axis), (**B**) α-PbO_2–type TiO_2 [the former can transform to the latter by 1/2[0$\bar{1}$1] shear for every other hcp plane (011)], and (**C**) the basic unit of α-PbO_2–type TiO_2 at the rutile twin boundary. Solid circles and open circles denote Ti and O atoms, respectively.

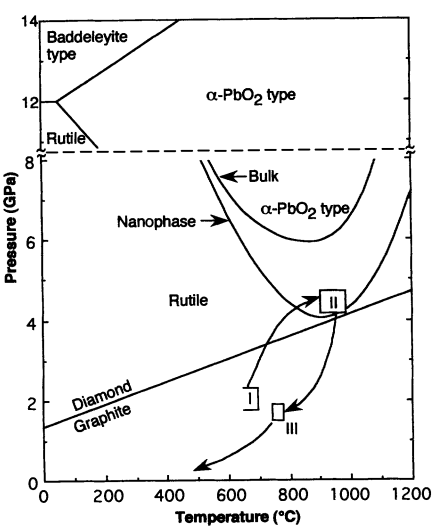

Fig. 4. *P-T* evolution of metamorphic stages I to III for the diamondiferous gneiss from the Erzgebirge (*7*). Also shown are the graphite-diamond transition (*19*), the phase boundary of rutile/α-PbO_2–type TiO_2 (*17*), and the phase boundary of baddeleyite/α-PbO_2–type TiO_2 (*22*).

type TiO_2 boundary (*17*) can be used to determine the pressure and temperature of the rock in the diamond stability field. In the present case, the subduction limit is close to the graphite-diamond boundary, but it may be different in other cases because of different temperature conditions and the envelope shape of the rutile–α-PbO_2 phase boundary. The baddeleyite/α-PbO_2–type TiO_2 boundary (*22*) could be a useful indicator of possible subduction to the transition zone of the mantle if baddeleyite-type TiO_2 can be preserved in a host of minerals with a high bulk modulus, such as diamond.

References and Notes

1. J. G. Liou, R. Y. Zhang, W. G. Ernst, D. Rumble III, S. Maruyama, *Rev. Mineral.* **37**, 33 (1998).
2. C. Chopin, *Contrib. Mineral. Petrol.* **86**, 107 (1984).
3. N. V. Sobolev and V. S. Shatsky, *Nature* **343**, 742 (1990).
4. H. J. Massonne *et al.*, *Eur. J. Mineral.* **10**, 497 (1998).
5. S. Xu *et al.*, *Science* **256**, 80 (1992).
6. L. F. Dobrzhinetskaya *et al.*, *Geology* **23**, 597 (1995).
7. H. J. Massonne, in *Proceedings of the 7th International Kimberlite Conference* (Cape Town, South Africa, April 1998), in press. The *P-T* conditions of three different stages of metamorphism of the quartzofeldspathic rocks from the Saxonian Erzgebirge were derived on the basis of the chemical zonation of garnet and phengite. The first stage is characterized by pressure conditions around 2 GPa at temperatures of about 700°C. The second stage is characterized by burial of the diamondiferous gneisses to depths of at least 130 km, which is suitable for diamond formation. Temperature between 900° and 1000°C were reached, as evidenced by introduction of Ti in the garnet. (A semiquantitative approach to metamorphic temperatures was taken using the Ti contents in Al-garnet coexisting with rutile and a SiO_2 phase. To ensure that he had plausible temperatures, Massonne compared his estimated data to metamorphic temperatures from the literature for the range from 600° to 1400° C.) Subsequent exhumation of the diamondiferous gneisses was accompanied by cooling. During this process, microdiamonds were enclosed in garnet before they could be completely graphitized. The third stage was characterized by phengite formation at temperatures around 750°C and pressures between 2 and 1.5 GPa.
8. A. Kriner and A. P. Willner, *Mineral. Petrol.* **132**, 1 (1998).
9. We used a JEOL 3010 instrument at 300 keV for imaging, electron diffraction, and point-count EDX of the argon-ion milled thin foils, which were supported by a molybdenum grid and a copper ring. To diminish beam-spreading effects, we used the smallest size (5 nm) and highest energy (300 keV) of the electron beam available with this instrument for EDX analysis at the thin area (<200 nm thick) of the specimen. Under such conditions, the x-ray spatial resolution was calculated to be 12 nm according to the single-scattering model [see D. B. Williams and C. B. Carter, *Transmission Electron Microscopy—Spectrometry IV* (Plenum, New York, 1996), p. 623; S. J. B. Reed, *Ultramicroscopy* **7**, 405 (1982)]. Therefore, with the α-PbO_2–structured TiO_2 slab (8 nm thick) edge-on, there was likely a considerable volume fraction of the slab analyzed out of total TiO_2 (i.e., α-PbO_2–structured TiO_2 slab plus rutile).
10. The angles between zone-axis patterns read from a Wulff net plotted with the double tilting angles of the AEM specimen holder are 19.5° ± 0.5° for [110]/[210], 8.5° ± 0.5° for [210]/[310], and 21.5° ± 0.5° for [310]/[100], in close agreement with the angles 19.2°, 9.1°, and 21.8°, respectively, calculated from the lattice parameters and orthorhombic indices of synthetic α-PbO_2–structured TiO_2 (*11*).
11. P. Y. Simons and F. Dachille, *Acta Crystallogr.* **23**, 334 (1967).
12. B. G. Hyde and S. Andersson, *Inorganic Crystal Structures* (Wiley, New York, 1989), pp. 67–72.
13. The eight *d*-spacings measured from Fig. 2 and compiled in Table 1 were used for least-squares refinement of the lattice parameters. The error of the *d*-spacing measurements on SAED patterns taken at a camera length of 150 cm and with rutile reflections in the same negatives as standard was estimated to be ±0.002 nm.
14. For example, 010 and 011 (actually 01*l*) diffractions are forbidden, as shown in Fig. 2D. Other systematic absences, such as 001 and 120, were confirmed by tilting to a systematic row of spots to avoid double diffractions. The nonforbidden spots were also confirmed in this way.
15. See T. Hahn (Ed.), *International Tables for Crystallography, Vol. A, Space Group Symmetry* (Reidel, Dordrecht, Netherlands, 1987), pp. 190–321.
16. K. Kusaba, M. Kikuchi, K. Fukuoka, Y. Syono, *Phys. Chem. Miner.* **15**, 238 (1988).
17. J. S. Olsen, L. Gerward, J. Z. Jiang, *J. Phys. Chem. Solids* **60**, 229 (1999). This phase boundary was recently determined by in situ x-ray powder diffraction using a synchrotron radiation source during heating and compression experiments in the multianvil device for bulk and nanophase material. When plotted in a *P-T* diagram, the rutile/α-PbO_2–type TiO_2 phase boundary changes from a negative to a positive slope with increasing temperature at ~6 GPa and 850°C for bulk material and at ~4 GPa and 900°C for nanophase material. The topology of the TiO_2 phase diagram is so similar to that of iron that the slope change of the phase boundary may be due to entropy change in either the rutile or the α-PbO_2–type phase, analogous to spin ordering at Curie transition for the iron phase with body-centered cubic structure. The curvature and change of slope went undetected in an earlier study [M. Akaogi *et al.*, in *Program and Abstracts of Papers Presented at the 30th High-Pressure Conference of Japan*, Y. Syono, Ed. (Japan Society of High Pressure Science and Technology, Kyoto, 1989), p. 111 (in Japanese)], possibly because of sluggishness of the transition at temperatures lower than 800°C.
18. Thermodynamically, the surface energy contribution to the energetics of a solid-solid transformation increases with decreasing crystal size. Because the size dependence of surface energy is different for different phases, the change in transition pressure with crystal size can be either way, depending on the system under investigation (*17*). In the case of CdSe, the transition from a wurtzite to a rock salt structure takes place at a higher pressure for nanocrystals than for the bulk [see S. H. Tolbert and A. P. Alivisatos, *Science* **265**, 373 (1994)]. As for the case of titania, the transformation pressure is lower for nanophase material than for the bulk, although the underlying mechanism has yet to be clarified (*17*).
19. R. G. Berman, in *The Properties of Diamond*, J. E. Field, Ed. (Academic Press, London, 1979), pp. 4–22.
20. A. N. Winchell and H. Winchell, *Elements of Optical Mineralogy—An Introduction to Microscopic Petrography* (Wiley, New York, ed. 4, 1961), p. 66.
21. D. G. Issak, J. D. Carnes, O. L. Anderson, H. Cynn, E. Hake, *Phys. Chem. Miner.* **26**, 31 (1998).
22. J. Tang and S. Endo, *J. Am. Ceram. Soc.* **76**, 796 (1993).

23. We thank H. J. Massonne for supplying the diamondiferous gneiss sample and unpublished results, L. J. Wang for her technical assistance on AEM, and referees for constructive comments. Supported by National Science Council, Taiwan, ROC (S.-L.H., P.S.).

17 February 2000; accepted 2 March 2000

The Influence of Canadian Forest Fires on Pollutant Concentrations in the United States

Gerhard Wotawa[1]*† and Michael Trainer[2]

High carbon monoxide (CO) concentrations from uncertain origins occurred episodically in the southeastern United States during the summer of 1995. We show that these episodes were caused by large forest fires in Canada. Over a period of 2 weeks, these natural emissions increased CO concentrations in the southeastern United States as well as along the eastern seaboard, a region with one of the world's highest rates of anthropogenic emissions. Within the forest fire plumes, there were also high concentrations of ozone, volatile organic compounds, and aerosols. These results suggest that the impact of boreal forest fire emissions on air quality in the mid-latitudes of the Northern Hemisphere, where anthropogenic pollutant sources have been considered predominant, needs to be reevaluated.

Forest fires are known to be a major source of CO and other air pollutants on a global scale (*1*). Large forest fire plumes, however, have been found mostly in tropical regions and above the oceans (*2*, *3*). A number of studies dealing with the influence of fires in boreal forests on trace gas concentrations in high northern latitudes were conducted as part of the NASA Arctic Boundary Layer Expeditions (*4*, *5*). It was shown that summertime sub-Arctic haze events were primarily a result of forest fires (*6*), that fires, together with stratospheric intrusions, contribute a major fraction of total oxidized nitrogen species (NO_y) in the remote sub-Arctic troposphere (*7*), and that these fires provide a net source

[1]University of Agricultural Sciences, Institute for Meteorology and Physics, Tuerkenschanzstrasse 18, A-1180 Vienna, Austria. [2]National Oceanic and Atmospheric Administration (NOAA) Aeronomy Laboratory, 325 Broadway, Boulder, CO 80303, USA.

*Visiting scientist at CIRES, University of Colorado, and NOAA Aeronomy Laboratory.

†To whom correspondence should be addressed. E-mail: gerhard.wotawa@boku.ac.at